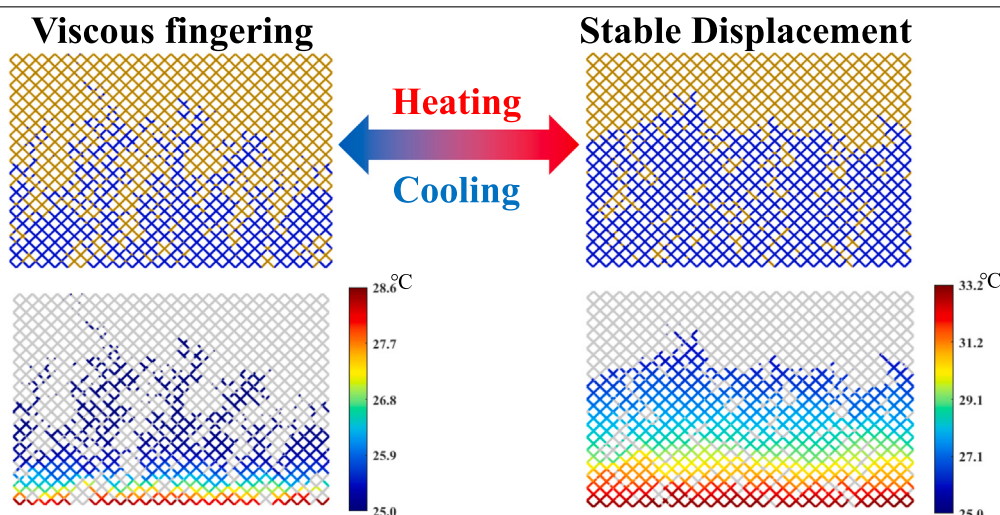


A computational model for pore-scale flow regime tuning with thermally responsive surfactants

Amirhosein Sarchami^{ID}, Kishan Bellur^{ID *}

Department of Mechanical and Materials Engineering, University of Cincinnati, Cincinnati, OH, USA

GRAPHICAL ABSTRACT



HIGHLIGHTS

- Injection rate and contact angle govern invasion and saturation in porous media.
- Isothermal surfactants enhance saturation at low flow rates via wettability change.
- Thermoresponsive surfactants shift flow from fingering to stable displacement.

ARTICLE INFO

Keywords:

Pore-scale modeling
Porous media transport
Two-phase flow
Thermally responsive surfactants

ABSTRACT

Recent experiments with temperature-sensitive surfactants have demonstrated the ability to reversibly toggle the wettability of an oil-water system. This novel curvature switching mechanism changes the direction of capillary pressure and as a result influence pore scale transport. This mechanism has the potential for active control of porous media transport mechanics. To that effect, a dynamic pore network model is developed to couple multiphase flow with thermal transport. The model accounts for temperature-sensitive surfactant-driven curvature switching and explores its impact on flow regimes, wettability, and interfacial tension. Simulations were conducted where a hydrophobic oil saturated porous network was injected with water (with and without surfactants). Initial simulations without surfactants or thermal effects show that higher

* Corresponding author.

E-mail address: bellurkn@ucmail.uc.edu (K. Bellur).

injection rates favor viscous fingering, while lower rates promote capillary fingering. Isothermal surfactant flooding reduces capillary forces by altering both surface tension and contact angle. This partially stabilizes the invasion front and increases network saturation by up to 30% for unfavorable mobility ratios ($M < 1$) at low injection rates. However, at higher injection rates, isothermal surfactants become less effective, and the viscous fingering regime remains largely unchanged. We report that using temperature-sensitive surfactant flooding, the flow pattern could be successfully altered. An otherwise viscous fingering regime could be converted to stable displacement under moderate heat loads ($Q_t = 0.05 \text{ W}$), leading to a 31.2% increase in network saturation. However, excessive heating ($Q_t = 0.1 \text{ W}$) reintroduces fingering near the inlet due to elevated capillary pressures. These results demonstrate that heat rates influence the pore scale displacement, allowing for programmable switching between viscous fingering to stable displacement for appropriate temperature-sensitive surfactants. This study highlights the potential of temperature-sensitive surfactants to optimize multiphase transport in porous materials, offering insights for applications in enhanced oil recovery, microfluidics, and beyond.

| Nomenclature | | Superscripts/Subscripts |
|----------------------|--|---|
| Acronyms | | |
| 2D | Two-dimensional | <i>i, j</i> Pore or node index |
| CF | Capillary fingering | <i>ij</i> Throat connecting pores <i>i</i> and <i>j</i> |
| CMC | Critical micelle concentration | <i>eff</i> Effective |
| DNS | Direct numerical simulation | <i>g</i> global |
| IMPES | Implicit pressure explicit saturation | <i>s</i> Solid |
| LBM | Lattice Boltzmann method | <i>t</i> Throat |
| LS | Level set | <i>T</i> Thermal |
| PNM | Pore network modeling | <i>n</i> Time step |
| SD | Stable displacement | |
| VF | Viscous fingering | |
| VoF | Volume of Fluid | |
| $C_{18}\text{TAB}$ | Octadecyl-trimethyl-ammonium bromide | Numbers |
| $C_{16}\text{OH}$ | Hexadecanol | 1 Defending fluid |
| Symbols | | 2 Invading fluid |
| A_c | Inlet cross-section area (cm^2) | |
| C_p | Specific heat ($\text{J/g } ^\circ\text{C}$) | |
| Ca | Capillary number (-) | |
| ΔP | Pressure difference (dyn/cm^2) | |
| K | Permeability (cm^2) | |
| k | Thermal conductivity ($\text{W/cm } ^\circ\text{C}$) | |
| L | Throat length (cm) | |
| M | Viscosity ratio (-) | |
| P_c | Capillary pressure (dyn/cm^2) | |
| Pe | Péclet number (-) | |
| Q | Injection rate (cm^3/s) | |
| \dot{Q} | Conduction heat transfer (W) | |
| q | Local volumetric flow rate (cm^3/s) | |
| R | Thermal resistance ($^\circ\text{C/W}$) | |
| S | Fraction of the liquid phases inside the throat (-) | |
| T | Temperature ($^\circ\text{C}$) | |
| x | Meniscus position (cm) | |
| Greek symbols | | |
| μ | Viscosity (Poise) | |
| v | Void space volume (cm^3) | |
| ρ | Density (g/cm^3) | |
| σ | Surface tension (dyn/cm) | |
| θ | Contact angle ($^\circ$) | |
| ϵ | Porosity (-) | |

1. Introduction

Two-phase flow in porous media has been a major focus of research over the last two decades, driven by the diverse flow patterns that arise from variations in viscosity, wettability, interfacial tension, and displacement rate [1]. Two-phase porous transport finds applications in various fields, including oil recovery [2], hydrology [3], geothermal energy extraction [4], CO_2 sequestration [5], contaminant transport [6], fuel cell [7], food and textile industries [8,9], and biomedical engineering [10].

Investigating transport in porous media is challenging due to pore morphology and environmental conditions. Experimental methods (e.g., micro-CT, SEM/TEM) offer great insight but are often cost and time prohibitive. The results are also sensitive to material properties, sample preparation, and testing conditions. Analytical solutions are typically limited to idealized systems with steady-state and specific boundary conditions, which restricts their real-world applicability [11,12]. As a result, numerical approaches have emerged as a reliable alternative. These methods provide a cost-effective and precise means to predict local transport phenomena (e.g., diffusion and permeation) while enabling systematic variations in parameters such as pore geometries, fluid properties, and boundary conditions.

Traditional numerical approaches based on Darcy theory fails to adequately capture pore-scale phenomena such as dynamic capillary effects, fluid-fluid interface movements, and wettability changes. Advanced numerical microscale modeling is needed to address these complexities [2,13]. Pore-scale models for two-phase flow can generally be classified into three main categories: (1) direct numerical simulation (DNS), (2) lattice Boltzmann method (LBM), and (3) pore network modeling (PNM). DNS methods, such as volume-of-fluid (VoF) and level-set (LS) [14,15], explicitly resolve pore structures and fluid dynamics. DNS is capable of simulating flow in any pore space geometry without requiring geometric simplifications. However, DNS

methods are computationally intensive for micro- and nanoscale domains. In capillary-dominated flows, DNS methods often suffer from numerical errors caused by inaccurate approximations of fluid–fluid interface curvatures, resulting in spurious currents [1]. LBM [16] operates at the mesoscale. It treats the fluid as particles that move and collide on a lattice grid, making it especially suitable for complex fluid dynamics problems in porous materials. While LBM provides a computationally efficient alternative to DNS, it becomes inefficient for systems with tens or hundreds of interconnected pores in each direction, as it is both time-consuming and limited to small pore volumes [17]. PNM simplifies the pore space into a network of interconnected nodes (pores) and links (throats) with idealized geometries. This enables the explicit calculation of simplified physics, such as the relationships between saturation, capillary pressure, and phase conductance [18,19]. With its simplified geometries and physics, PNM can simulate over larger domains with significantly reduced computational requirements. With key flow dynamics effectively represented by local rules within pore bodies and throats, PNM offers valuable insights into both pore-scale flow behavior and its macroscopic implications. The pore-network model, first introduced by Fatt in 1956 [18], featured a regular two-dimensional (2D) topology. Since then, this modeling approach has undergone significant refinement and is now widely applied in fields such as petroleum engineering, hydrology, soil physics, and industrial porous media studies [20–23].

The wetting characteristics play an important role in determining the location, flow, and distribution of fluids. This is a result of the interaction between the fluids and the attractive forces on the wall. When two immiscible fluids coexist in porous materials, the relative surface tensions between the three phases, namely the two fluids and the solid, determine the wettability commonly characterized by the contact angle. Wetting is critical to two-phase flow in porous media as it determines both the direction and the magnitude of intrinsic capillary pressure. Imbibition is the process where a wetting fluid displaces a non-wetting fluid. In contrast, drainage occurs when a non-wetting fluid displaces a wetting fluid. Modification of wettability results in significant variations in fluid behavior and affects overall transport mechanics in imbibition and drainage processes [24,25]. Hammond and Unsal [26] developed a dynamic pore network model that predicts oil displacement in porous media employing a surfactant solution, which alters wettability and reduces interfacial tension. This model effectively couples the dynamics of oil displacement with surfactant transport, illustrating how surfactant-induced changes in wettability can stabilize displacement fronts in porous media. They also developed an experimental setup to study oil displacement through wettability-modifying surfactants, showing that the presence of surfactants modified wettability and improved oil displacement [23]. Surfactants are also commonly used in hydraulic fracturing to boost fluid recovery. Sun et al. [27] investigated the performance of betaine surfactant, by analyzing its influence on interfacial tension and wettability. They developed a network model with adjustable fracture widths to simulate complex reservoir conditions. Experiments were also conducted to evaluate the impact of surfactant concentration, permeability, and temperature on oil recovery during dynamic imbibition. Their results demonstrated that oil recovery improved 22.6% when 0.5 wt% surfactant was used. The effects of capillary, viscous, and gravity forces, along with wettability changes during surfactant flooding, have been extensively studied [28–31]. The findings indicated that low interfacial tension is critical for balancing capillary forces and affecting the dynamics of oil recovery.

While previous numerical and experimental works have provided valuable insights into the alteration of wettability and the effects of changing the surface tension through surfactants in two-phase flow within porous media, they have not yet explored the ability to actively control wettability and consequently tune the flow pattern. Controlling the curvature of the meniscus is critical for a variety of applications,

including liquid lens technologies [32], interfacial assembly [33], microfluidics [34], 3D printing [35], thermal management [36], and microelectronic device fabrication [37]. While existing methods allow for curvature control by altering the chemical composition of the sample [38], surface treatments [39,40] or applying external fields [41] the reversible switching of meniscus curvature between concave to convex states by adjusting temperature has not been thoroughly investigated, especially in the context of porous transport.

In this study, the two-phase flow in porous materials is modeled using a dynamic pore network method that couples two-phase flow with thermal transport dynamics. A novel coupled thermal/flow model is designed to simulate a thermally actuated change in the wettability and surface tension of menisci in immiscible flows. By incorporating this behavior into a two-way coupled flow/thermal pore-scale model, we aim to demonstrate how temperature-induced wettability changes can enhance transport behavior in porous media, offering new insights into optimizing flow processes for various applications. While prior drainage studies [42] have shown that regime transitions between viscous fingering, capillary fingering, and stable displacement are governed by flow rate, length scale, and fluid/substrate combinations, our work emphasizes that equivalent transitions can be achieved solely through *in-situ thermal control*. This introduces a fundamentally new axis of control for displacement behavior in porous media, without the need to alter flow conditions or materials.

2. Curvature switching

Recent work by Shool et al. [43] reported a reversible, thermally induced transition in the curvature of the oil–water meniscus in surfactant-laden capillary systems. This phenomenon, herein referred to as *curvature switching*, involves a gradual transition between concave and convex meniscus shapes as temperature is varied (Fig. 1). This, in turn, alters capillary pressure in both direction and magnitude. This behavior poses a challenge to traditional PNM approaches where capillary pressure is typically assumed to be independent of temperature. The underlying physics of curvature switching is governed by two key mechanisms:

(1) *interfacial freezing at the oil–water interface*. At lower temperatures (near the freezing point), a crystalline monolayer can form at the oil–water interface. When this monolayer is formed, the slope of surface tension vs. temperature changes from slightly negative to strongly positive [43]. This interfacial freezing point is tunable via the concentration of a suitable surfactant, which alters the freezing temperature and hence modifies surface tension as a function of temperature.

(2) *temperature-dependent adsorption of C₁₈TAB*. On the water side, the adsorption–desorption of C₁₈TAB surfactant to the capillary wall is temperature sensitive. As temperature increases, more surfactant adsorbs to the wall, altering the local wettability and requiring a shift in contact angle to satisfy Young's equation. This wetting change further contributes to meniscus curvature transitions.

When combined, the two effects described above enable dynamic, reversible control over both surface tension and contact angle, and consequently the ability to tune capillary pressure as a function of temperature. To validate this behavior, we conducted experiments using DI water with C₁₈TAB and hexadecane with hexadecanol surfactant solutions in borosilicate capillaries. Surfactant concentrations were kept above the critical micelle concentration (CMC) to eliminate concentration-dependent effects. A series of high-resolution images captured during controlled heating (25–45 °C) confirmed the curvature switching, as shown in Fig. 2. The meniscus transitions from concave (hydrophilic) to convex (hydrophobic), with a temperature scale bar provided for reference. During this heating process, a linear decrease in contact angle θ was observed; transitioning from 120 ± 5° (hydrophilic) to 18 ± 5° more hydrophobic values (Fig. 3). Meanwhile, surface tension (σ) data reproduced from Shool et al. [43] shows an almost

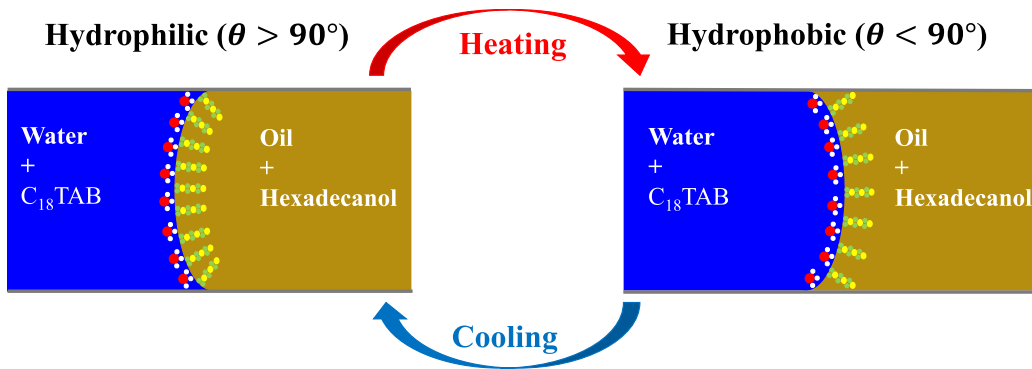


Fig. 1. Schematic representation of the meniscus curvature inversion mechanism during heating and cooling. Water and oil (hexadecane) are mixed with C_{18} TAB and hexadecanol surfactants, respectively.

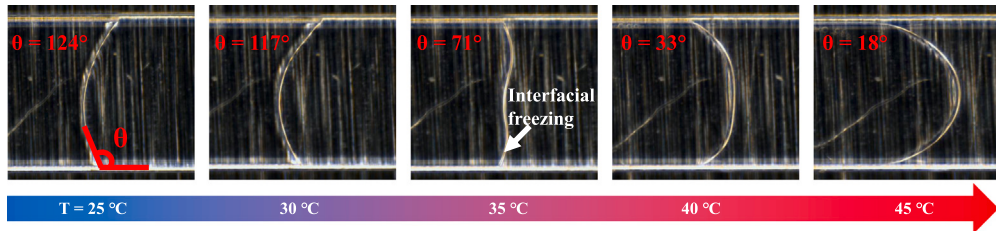


Fig. 2. Visualization of curvature switching in a single capillary tube with water + C_{18} TAB on the left and hexadecane + hexadecanol on the right. Images show a transition from concave to convex curvature as temperature increases. The color bar indicates local throat temperature.

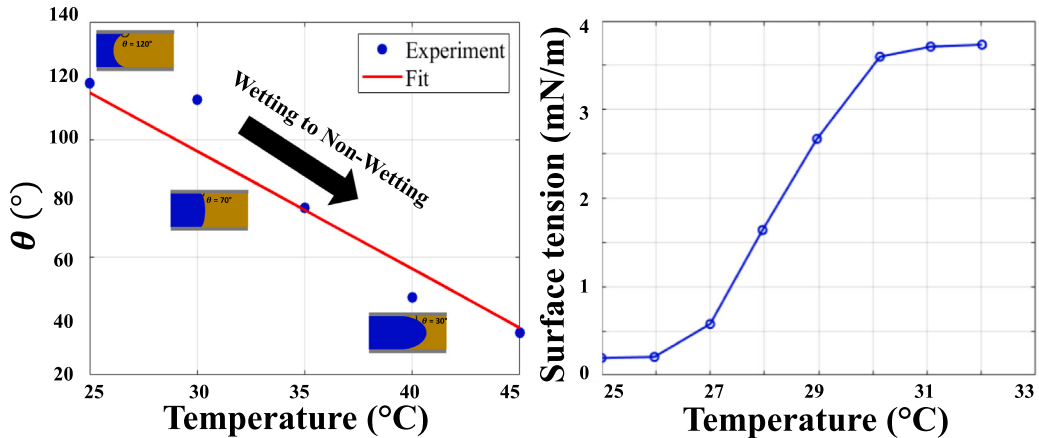


Fig. 3. Variation of contact angle (θ) from our experiments and surface tension (σ) from Shool et al. [43] with temperature.

linear increase between 27–30 °C, with minimal change outside this range. Uncertainty in σ is ± 0.2 mN/m.

The experimental results reveal that both surface tension and contact angle can be dynamically tuned, leading to thermally induced curvature switching. These findings highlight the need to incorporate thermal effects and interfacial property variations into pore-scale flow models. In the following section, we develop a coupled two-phase flow and thermal pore network model that accounts for temperature-dependent interfacial phenomena. The goal is to understand how local changes in capillary pressure driven by curvature switching influence global fluid transport behavior within porous structures.

3. Coupled two-phase flow/thermal modeling

3.1. Construction of the pore network

The computational domain is represented as a network of cylindrical tubes based on a given pore size distribution. At each node (pore),

four throats intersect. No volume is assigned to the pores themselves. Instead, the entire pore volume is accounted for by the throats (Fig. 4). Each throat is modeled as a cylinder with uniform length L , and its radius r is randomly chosen based on a uniform distribution from the interval $[\lambda_1 L, \lambda_2 L]$, where $0 < \lambda_1 < \lambda_2 < 1$. This randomness in radii introduces disorder, reflecting the heterogeneous nature of real porous media, where throat sizes vary. The parameters λ_1 and λ_2 control the distribution width of the throat radii.

3.2. Two-phase flow model

In this work, the implicit-pressure explicit-saturation (IMPES) formulation is used for dynamic PNM simulations due to its balance between computational efficiency and accuracy [44]. Dynamic PNM accounts for transient fluid transport behavior and interface movement within the network. Invading and defending fluids are assumed to be incompressible and immiscible, forming a well-defined interface.

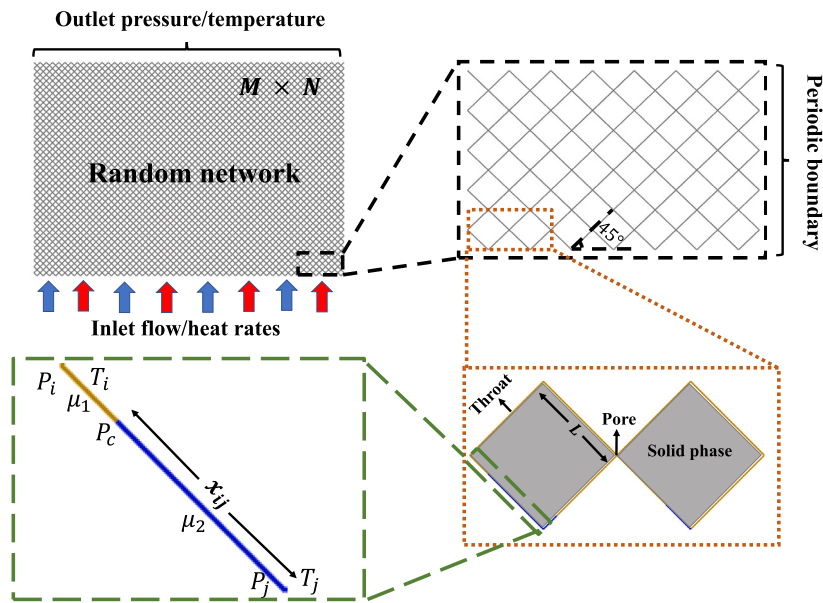


Fig. 4. A random network including cylindrical throats interconnected at pores is constructed. The blue, brown, and gray colors in the invaded network correspond to the invading and defending fluids and solid phase, respectively.

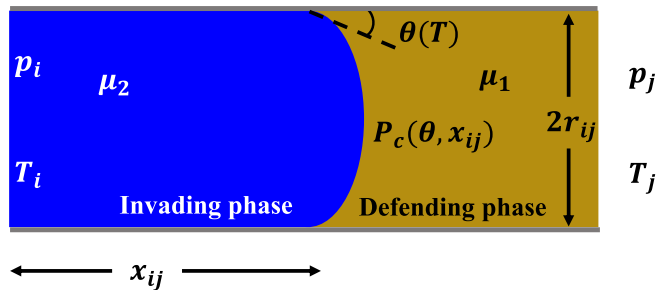


Fig. 5. Two-phase flow in a throat containing an immiscible interface. The yellow-colored liquid on the right represents the defending phase and the blue-colored liquid on the left represents the invading phase. This configuration represents a defending phase wetting system with $\theta < 90^\circ$.

Consider a throat containing both fluids between nodes i and j within the network (Fig. 5). The capillary pressure P_c across the interface is governed by the Young-Laplace equation:

$$P_c = \frac{2\sigma \cos \theta}{r_{ij}} \quad (1)$$

where θ is the contact angle as measured through the defending phase, and r_{ij} represents the local throat radius. The volumetric flow rate q_{ij} through the throat connecting the i th node to the j th node is derived based on the Washburn equation [45]:

$$q_{ij} = - \left(\frac{\pi r_{ij}^2 K_{ij}}{\mu_{\text{eff}} L} \right) (\Delta p_{ij} - P_c). \quad (2)$$

The permeability, $K_{ij} = \frac{r_{ij}^2}{8}$ and Δp_{ij} is the difference in pressure between the i th and j th nodes. The effective viscosity, μ_{eff} , is calculated as the weighted sum of the viscosities of the individual fluids, based on the proportions of each fluid present in the throat (represented by x_{ij}):

$$\mu_{\text{eff}} = \mu_2 \frac{x_{ij}}{L} + \mu_1 \left(1 - \frac{x_{ij}}{L} \right). \quad (3)$$

Within a throat, two primary scenarios can occur: it may be entirely occupied by either the defending or invading phases, or it may be partially filled with both fluids. When partially filled, one or two

menisci may be present, leading to six distinct arrangements (Fig. 6). Menisci position can vary anywhere between the ends of the throat, and their movement can be bidirectional. The magnitude of the capillary pressure for a single meniscus is defined by Eq. (1), while its sign is dictated by the orientation of the meniscus, which can either point upward (Fig. 6(c)) or downward (Fig. 6(d)), dictated by the applied pressure gradient and contact angle. In the absence of menisci in the throat (Fig. 6(a and b)), P_c is set to zero, and Eq. (2) is simplified to the form corresponding to Hagen-Poiseuille flow, with μ_{eff} given by μ_1 or μ_2 .

To accurately capture the impact of temperature-sensitive surfactants on wettability, it is necessary to track the temperature distribution throughout the network. By coupling a thermal transport model with the two-phase flow, the dynamic interactions between temperature and wettability can be captured. This provides a comprehensive framework for analyzing transport behavior in porous media. The following section details the development of this thermal model and its integration with the flow model.

3.3. Thermal model

The thermal transport model used in this study is similar to the one proposed by Surasani et al. [46], in which heat transfer occurs exclusively through conduction between nodes. Convective heat transfer between the solid phase and the liquids is neglected due to the low Reynolds number (Re) associated with each throat across the network. This assumption is further justified by the thermal Péclet number which quantifies the ratio of the advective to the diffusive heat transport. In most of our simulations, the thermal Péclet number is on the order of 10^{-2} indicating that advection has a negligible contribution compared to thermal diffusion. Energy conservation is applied around node i assuming conduction only heat transfer:

$$(v\rho C_p)_j \frac{dT_j}{dt} = \sum_{j=1}^4 \dot{Q}_{ij}, \quad (4)$$

Here, \dot{Q}_{ij} is the conduction heat transfer and the left-hand side term describes the transient heat storage. The quantity $(v\rho C_p)_j$ is the total heat capacity at each node, which depends on the heat capacity of the solid phase and the volumes of the defending (1) and invading (2)

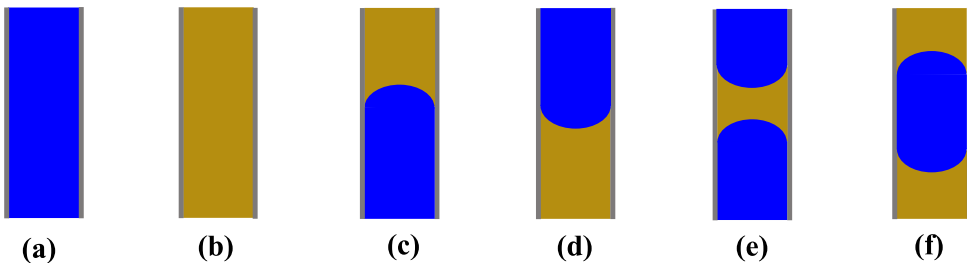


Fig. 6. Six distinct fluid arrangements are possible within a single throat. (a) and (b) describe single phase flow where $P_c=0$. (c) and (d) represent a single meniscus. (e) and (f) represent multiple menisci resulting in “slugs”.

fluids. The total heat capacity is calculated using:

$$(v\rho C_p)_j = \frac{L}{2} \sum_{j=1}^4 \left\{ [\pi r_{ij}^2 (\frac{1}{\epsilon} - 1)](\rho C_p)_s + S_{ij} \pi r_{ij}^2 (\rho C_p)_2 + (1 - S_{ij}) \pi r_{ij}^2 (\rho C_p)_1 \right\}, \quad (5)$$

where S_{ij} is defined as the fraction of invading fluid present in the throats, and ϵ represents the porosity [7]. The total heat conduction, \dot{Q}_{ij} , between nodes i and j is expressed by:

$$\dot{Q}_{ij} = \frac{T_j - T_i}{R_{ij}}. \quad (6)$$

Here, T_i and T_j are the temperatures at nodes i and j , respectively. The effective thermal resistance is determined as a series/parallel sum of the solid and fluid phase resistances. The equivalent thermal resistance R_{ij} is:

$$R_{ij} = \frac{R_s [S_{ij} R_2 + (1 - S_{ij}) R_1]}{R_s + S_{ij} R_2 + (1 - S_{ij}) R_1}, \quad (7)$$

where R_s , R_2 , and R_1 are the thermal resistances of the solid, invading phase, and defending phase, respectively:

$$R_s = \frac{L}{k_s \pi r_{ij}^2} \left(\frac{\epsilon}{1 - \epsilon} \right) \quad (8)$$

$$R_2 = \frac{L}{k_2 \pi r_{ij}^2} \quad (9)$$

$$R_1 = \frac{L}{k_1 \pi r_{ij}^2}. \quad (10)$$

In Eqs. (8)–(10), k_s , k_2 , and k_1 are the thermal conductivities of the solid, invading fluid, and defending fluid, respectively. To explicitly calculate the temperature, an appropriate time step is required for convergence, which will be discussed in the following subsection.

The thermal pore network model is designed in a way that captures all six possible fluid arrangements shown in Fig. 6. The model explicitly tracks the local occupancy of each throat and integrates it into the heat transfer framework by updating the effective thermal resistance and heat capacity in real time. This approach allows Eqs. (5)–(7) to remain valid across a wide range of solid–liquid arrangements, regardless of the number or orientation of menisci. As the fluid distribution evolves, the model resolves transient heat conduction through both the solid matrix and the fluid phases, accounts for localized temperature gradients, and captures the effects of temperature on interfacial properties such as surfactant behavior and wettability.

3.4. Coupled numerical model

A coupled numerical model that integrates both flow and thermal transport is needed to accurately capture the impact of curvature switching in each throat on the flow pattern in the network. The flow model governs the fluid displacement and capillary pressure evolution within the network. The thermal model tracks the temperature distribution and its influence on interfacial properties. To fully account

for the curvature switching mechanism and its subsequent effect on flow behavior, it is essential to couple the flow and thermal models. The coupling ensures that temperature-dependent variations in contact angle and surface tension dynamically influence capillary pressure. This, in turn, changes the invasion pattern and transport characteristics within the porous structure. The coupling is achieved by making the contact angle θ and surface tension σ in Eq. (1) dependent on the throat temperature. The throat temperature T_t is calculated by averaging the temperatures of the connected nodes at the end of the previous time step. As a result, the capillary pressures of all throats with menisci can vary over time as the temperature evolves. In this work, fitted surface tension data from Shool et al. [43] and contact angle data from our experiments (Fig. 2) are used to relate both contact angle and surface tension to the throat temperature, as follows:

$$\theta_i = -5T_t + 245 \quad (11)$$

$$\sigma_i = -0.04T_t^3 + 3.48T_t^2 - 97.92T_t + 909.58 \quad (12)$$

where θ_i and σ_i are the contact angle and surface tension in a throat for each meniscus.

4. Numerical algorithm

4.1. Flow model solution

Assuming that the fluids are incompressible, we employ conservation of volume flux at each node:

$$\sum_j q_{ij} = 0, \quad (13)$$

here q_{ij} represents the flow through a throat connecting nodes i and j . The summation over j is performed over the nearest neighbor nodes (pores) of the i th node. The index i spans all internal nodes in the network, excluding those at the inlet or outlet of the network. The obtained system of linear equations is then solved under the constraint that the injection rate at the inlet and pressure at outlet nodes are held constant. By substituting Eq. (2) into Eq. (13), a vectorized expression for local pressure at internal nodes is obtained:

$$P_j = \sum_j (D^{-1})_{ij} B_i. \quad (14)$$

D is a conductance matrix, where the elements are dependent on the connections between different throats and their respective mobilities. P is a pressure vector represents the pressure at the internal nodes, while B_i accounts for the pressure at the boundaries (inlet and outlet) and the capillary pressure, if a meniscus is present in the throat.

According to Aker et al. [19], the injection rate is a function of pressure difference across the system, influenced by the medium's geometry and fluid configuration. The pressure difference across the network evolves over time at a fixed injection rate. The pressure difference across the network is then used to compute local flow rates within individual throats. The solution process involves calculating pressure for a given injection rate and using it to determine local flow

distributions, ensuring consistency with Eq. (13). Next, the positions of menisci during the invasion process within the network at each time step are updated. The time step is chosen to ensure a controlled displacement of the menisci that prevents excessive movement. During each step, if a meniscus reaches the end of a throat, the time step is adjusted so that it stops at the boundary before moving into the next throat. A second-order Runge–Kutta method is used for updating meniscus positions. Stability and convergence of the numerical solution are verified by monitoring pressure variations in the network. To accurately capture capillary pressure effects, the displacement length of menisci is controlled. The velocity at the midpoint of each time step is incorporated into the calculations to prevent excessive movement, ensuring numerical stability. The process is repeated iteratively until the displacements remain within an acceptable limit, no more than 10% of the tube length ($\Delta x_{\max} \leq 0.1L$). Once the menisci are updated, the total elapsed time is recorded, and nodal pressures are recalculated based on the new fluid configuration. When a meniscus reaches the end of a throat, it transitions into neighboring throats based on predefined rules [19]. The key rules are summarized below (additional details in the supporting information):

- A meniscus that approaches a node is equally split into the neighboring throats by introducing three new menisci. This is typically 1%–5% of the throat length and is governed by the time step.
- Next, the volume conservation (Eq. (13)) is applied to update the meniscus location. The meniscus is allowed to retreat if $\Delta P_{ij} < P_{c_{ij}}$.
- If a new meniscus is introduced into a throat already containing two menisci, they are merged to maintain consistency.

4.2. Thermal model solution

The solution for the thermal model is developed in a manner similar to the flow model. The dynamic energy balance at each node is explicitly solved by employing the current temperature field. The time step in the thermal model is the same as that used for the flow model, which is computed using a second-order Runge–Kutta scheme. For stability of the thermal model, the time step must be smaller than the maximum value of $(\nu\rho C_p)_i R_{ij}$ in the network, which is the product of node's total heat capacity and the effective thermal resistance of its neighboring throats, across the entire network. Thermal resistances for all three phases are calculated for each throat using Eqs. (8)–(10). Then, by applying a constant heat rate to the inlet of the network, the temporal temperature gradient of all nodes is determined based on Eq. (4). The equations are rewritten in matrix form by transferring all known parameters, including the updated total heat capacity, effective resistance, and fixed temperatures corresponding to the inlet and outlet nodes, to the right-hand side:

$$\sum_{j=1} D_{T,ij} \frac{dT_j}{dt} = B_{T,i}, \quad (15)$$

where, $D_{T,ij}$ is a sparse symmetric matrix, and $B_{T,i}$ is a vector of boundary conditions. The temperature for the next time step is then updated as follows:

$$T_j^{n+1} = \Delta t \left(\sum_{j=1} (D^{-1})_{ij} B_i \right) + T_j^n. \quad (16)$$

A procedure similar to that employed in the flow model is used to achieve the heat transfer rates in the throats based on the temperature differences (ΔT) across the network. At each step, the total heat capacity and effective thermal resistance are updated as functions of the throat's saturation.

4.3. Boundary and initial conditions

At the beginning of the simulation, the entire pore network is assumed to be saturated with a defending fluid (hexadecane) which has a viscosity of μ_1 . The invading fluid (water) with viscosity μ_2 is introduced at a constant injection rate from the bottom boundary of the network. Periodic boundary conditions are imposed on the side walls of the pore network. This allows the system to approximate an infinitely repeating structure in the horizontal direction. Zero gauge pressure is maintained at the top of the network representing the outlet.

In parallel, the thermal model considers a uniform heat rate applied at the bottom boundary of the network. Initially, all nodes within the saturated network are assigned a uniform temperature of 25 °C. Additionally, a fixed temperature of 25 °C is prescribed for all nodes located at the top boundary of the network. All other thermophysical properties were assumed to be temperature-independent due to their negligible variation within the temperature range of 25–45 °C.

4.4. Coupled flow/thermal model solution

The solution process starts with defining the input parameters: size of domain ($m \times n$), inlet flow rate, heat rate, viscosities of the liquids, throat length, thermal conductivity, specific heat capacity, density of the three phases, and the initial surface tension and contact angle (Fig. 7). Next, the flow model is executed to obtain the pressures at the nodes, and the flow rates/velocities at the throats. Using the calculated velocities for all throats, the invading phase is either advanced or retreated, and position-related variables are updated for the next time step. The thermal model then computes the temperatures at the nodes and the heat transfer rates through the throats. To couple the flow and thermal models, the temperature-dependent properties, such as θ and σ , are updated using Eqs. (11) and (12) as outlined in Section 2. With these updated properties, the capillary pressure (P_c) can now be recalculated. To ensure the stability of the numerical solution, the recalculated P_c is fed back to the flow model and the process is repeated until a converged temperature is obtained. Convergence is considered to be achieved when the temperature change is $< 1\mu\text{K}$ in successive iterations. Once convergence is reached, the model progresses to the next time step, and the process is repeated until a meniscus reaches the top surface (outlet), indicating breakthrough.

5. Results and discussions

Three main forces govern the two-phase flow through porous materials: viscous forces in the invading and defending fluids, and the capillary forces at the interface. These interactions are characterized by two dimensionless numbers: the capillary number (Ca) and the viscosity ratio (M). The capillary number signifies the ratio of capillary to viscous forces:

$$\text{Ca} = \frac{Q\mu}{A_c\sigma}. \quad (17)$$

Here, Q is the injection rate (m^3/s), μ is the maximum fluid viscosity ($\text{Pa}\cdot\text{s}$), A_c is the inlet cross-sectional area (m^2), and σ is the interfacial tension (N/m). The viscosity ratio M is given by:

$$M = \frac{\mu_2}{\mu_1}, \quad (18)$$

where μ_2 and μ_1 are the viscosities of the invading and defending fluids, respectively.

In the following sections, these dimensionless numbers are used to initially categorize flow regimes in the porous network. The effects of injection rate, and contact angle for each regime are then studied using the two-phase flow model with and without surfactants. First, surfactants are assumed to be temperature-insensitive, and isothermal simulations are conducted without the thermal model. Next, the coupled flow/thermal model is applied to explore the effect of

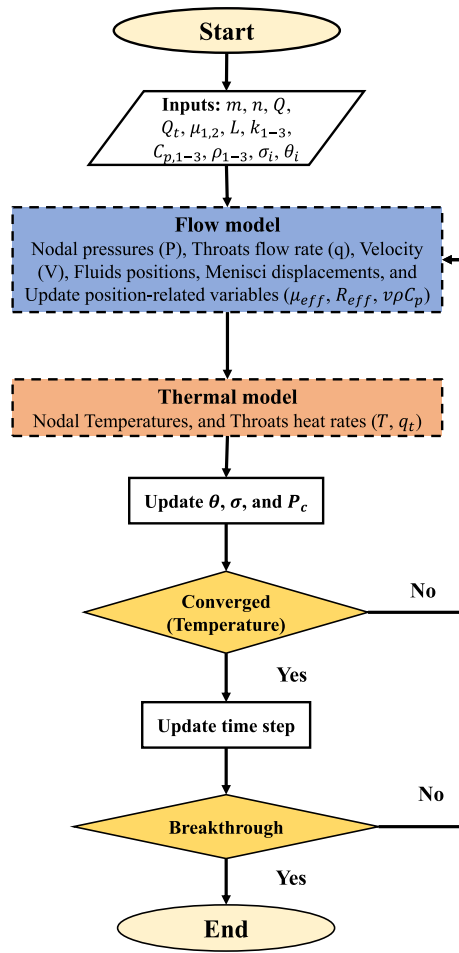


Fig. 7. Flowchart of the coupled flow/thermal model. The diagram shows the step-by-step procedure for simulating fluid invasion and heat transfer, starting from input initialization to the iterative coupling of pressure and temperature calculations. The process continues until the invading fluid breaks through the outlet.

temperature-sensitive surfactants and curvature-switching behavior on the invasion patterns.

5.1. Validation

5.1.1. Numerical validation

First, we validate our model in the three main flow regimes: the viscous fingering, stable displacement, and capillary fingering, with well known work by Aker et al. [19]. The throat lengths (L) were uniformly set to 0.1 cm, while throat radii (r) were randomly chosen within $0.05L \leq r \leq L$ using a uniform distribution. The thermal model was not included, only the two-phase flow model with constant contact angle and surface tension is solved. The surface tension and contact angle were set to $\sigma = 30$ dyne/cm and 0° (perfect wetting). Defending and invading fluid viscosities varied from 0.01 Poise (water) to 10 Poise (glycerol). In general, flow regime depends on both the capillary number (Ca) and viscosity ratio (M). However in this section we primarily vary M to obtain the different regimes: viscous fingering ($M < 1$), stable displacement ($M > 1$), and capillary fingering ($M = 1$). Both viscous fingering and stable displacement have the same Ca number, while the capillary fingering regime has a lower Ca number.

Fig. 8 shows the pressure evolutions and flow patterns for the different regimes. The top row is our data and the bottom row shows the corresponding data from Aker et al. [19]. Fig. 8(a) represents viscous

fingering on a 60×80 node network. The injection rate was $Q = 1.5$ ml/min, and viscosities were $\mu_2 = 0.01$ Poise and $\mu_1 = 10$ Poise, yielding $Ca = 4.6 \times 10^{-3}$ and $M = 1.0 \times 10^{-3}$. The invading fluid forms characteristic fingers, driven by viscous forces, while capillary forces play a smaller role. Due to the constant injection rate, the pressure across the lattice (ΔP) decreases as the less viscous fluid invades the system. The rate at which this pressure decreases is non-trivial and is expected to depend on the fractal development of the fingers. The rapid decrease at the end of the pressure plot corresponds to the breakthrough of the invading fluid. The global capillary pressure (P_{cg}) which is the sum of all capillary pressures across the network exhibits fluctuations as the menisci at the fingertips move through the tubes. Fig. 8(b) illustrates stable displacement regime on a 60×60 node network. In Aker et al. [19], the invasion process stopped when the invading fluid reached half the network, while our simulation continued until breakthrough. The injection rate was $Q = 1.5$ ml/min, with viscosities $\mu_2 = 10$ Poise and $\mu_1 = 0.10$ Poise, yielding $Ca = 4.6 \times 10^{-3}$ and $M = 1.0 \times 10^2$. In stable displacement, invading fluid's viscous forces dominate, stabilizing the front and creating a compact interface between fluids. The pressure across the network increases with the volume of high-viscosity invading fluid injected into the system. Similarly, the global capillary pressure increases but at a lower rate. This increase is caused by the viscous drag acting on the trapped clusters of defending fluid left behind the front. Fig. 8(c) shows a capillary fingering pattern across a 40×60 node network. The injection rate was $Q = 0.2$ ml/min, and both fluids had equal viscosities ($\mu_1 = \mu_2 = 0.50$ Poise), resulting in $M = 1.0$ and $Ca = 4.6 \times 10^{-5}$. In this regime, viscous forces are negligible, and capillary forces dominate. The invading fluid follows a random path of least resistance, dictated by the threshold pressures of the tubes. Fig. 8(c) shows a rough front with trapped clusters of defending fluid. The pressure across the network exhibits sudden jumps caused by capillary variations when the non-wetting fluid invades or retreats from a throat. All three regimes show very good agreement with Aker et al. [19].

5.1.2. Experimental validation

In addition to the numerical validation, another simulation was performed using parameters that closely matched the experiments conducted by Ferer et al. [47]. The network was initially saturated with water, and air was subsequently injected using a syringe pump ($M < 1$). The flow patterns at the same, where capillary number (2×10^{-5}) and injection rate (5 ml/min) were compared as illustrated by Fig. 9. It should be noted that the small differences between the patterns are due to the randomness introduced by the random number generator for the size distribution in the numerical modeling. The light gray color in the experimental flow pattern represents an earlier time interval, while the dark gray color represents the final finger reaching breakthrough. As shown, a viscous fingering pattern is expected at this large injection rate. The characteristic features of viscous fingering, including thin fingers and trapping, are clearly observed. The black scale indicates the final finger extended to breakthrough. Similarly, the numerical flow pattern also exhibits a viscous fingering structure, with thin fingers reaching the end of the network. In all cases, the flow model results compared well with previous well-known modeling and experimental studies.

5.2. Isothermal simulations without surfactants

Once the model was validated, additional simulations were performed to investigate the effects of varying the injection rate (Q), and contact angle ($\theta \leq 90^\circ$) on the phase saturation and invasion patterns. The flow regimes include viscous fingering (VF), stable displacement (SD), and capillary fingering (CF). Q varies from 0.0025 to 0.075 cm³/s for VF and SD, and from 0.0033 to 0.1 cm³/s for CF. θ also ranges from 0° to 90° .

In addition, both the network randomness and the size of the pore

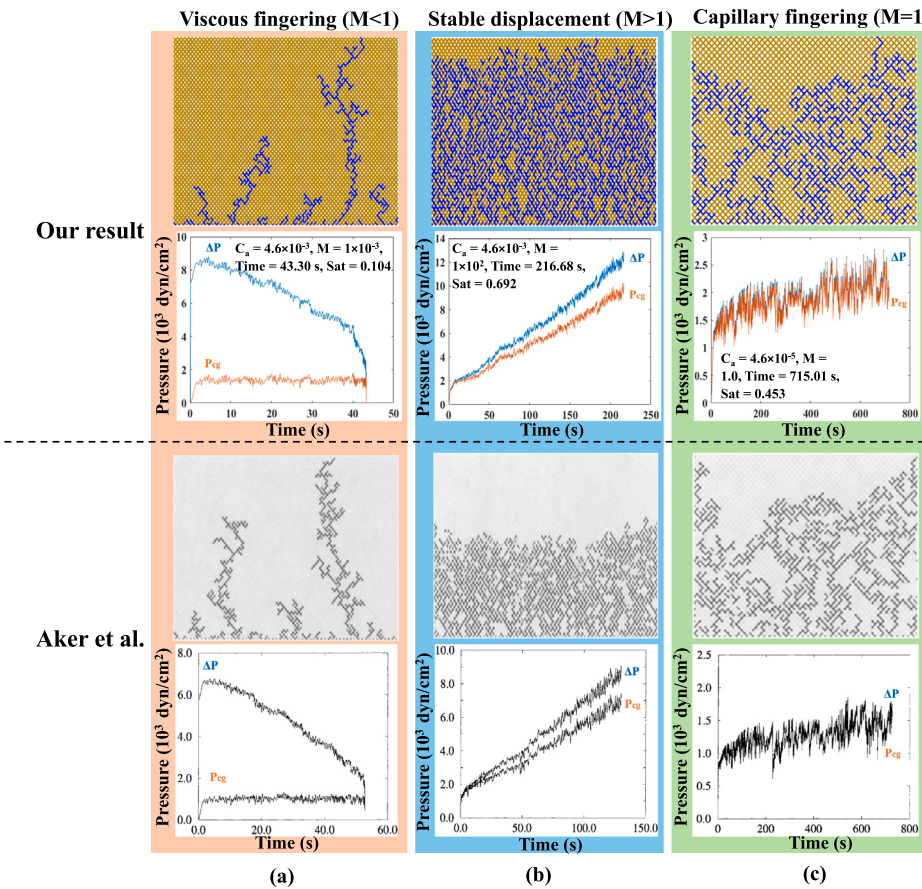


Fig. 8. Flow patterns and pressure evolutions for (a) $M = 1.0 \times 10^{-3}$ and $Ca = 4.6 \times 10^{-3}$, (b) $M = 1.0 \times 10^2$ and $Ca = 4.6 \times 10^{-3}$, (c) $M = 1.0$ and $Ca = 4.6 \times 10^{-5}$. All regimes are compared with Aker et al. simulations [19].

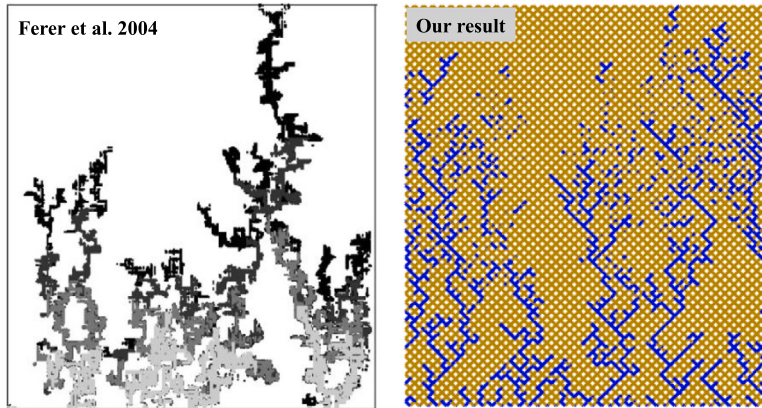


Fig. 9. Comparison between experimental results by Ferer et al. [47] and our modeling results for $Q = 5 \text{ ml/min}$, $M = 1.8 \times 10^{-3}$ and $Ca = 2 \times 10^{-5}$. Both cases show a similar viscous fingering pattern.

network were studied and resulted in have minimal influence on the qualitative flow behavior and regime classification across all cases studied (details in the supporting information). The consistency of pressure evolution and saturation trends, despite variations in pore connectivity and domain size demonstrates that the model captures the fundamental physics of multiphase displacement independent of specific geometric realizations. This robustness allows us to confidently use a smaller network than the validation network sizes with a single random seed in subsequent simulations. The goal moving forward is to systematically probe the impact of curvature switching on flow behavior. To achieve this efficiently, we adopt a simpler and computationally less expensive

network configuration that retains the essential physical features of the system while enabling extensive parametric studies.

5.2.1. Effect of injection rate

In this section, the effect of injection rate on network saturation, invasion pattern, and pressure variation is analyzed for different viscosity ratios. The network size is set to 25×35 , θ (contact angle) = 0° , and \hat{n} (seed number) is set to 0. Fig. 10(a) shows that higher injection rates or Ca lead to viscous fingering, reducing invasion phase saturation. Whereas at lower Ca , network saturation increases, and the regime transitions to capillary fingering. This is confirmed by

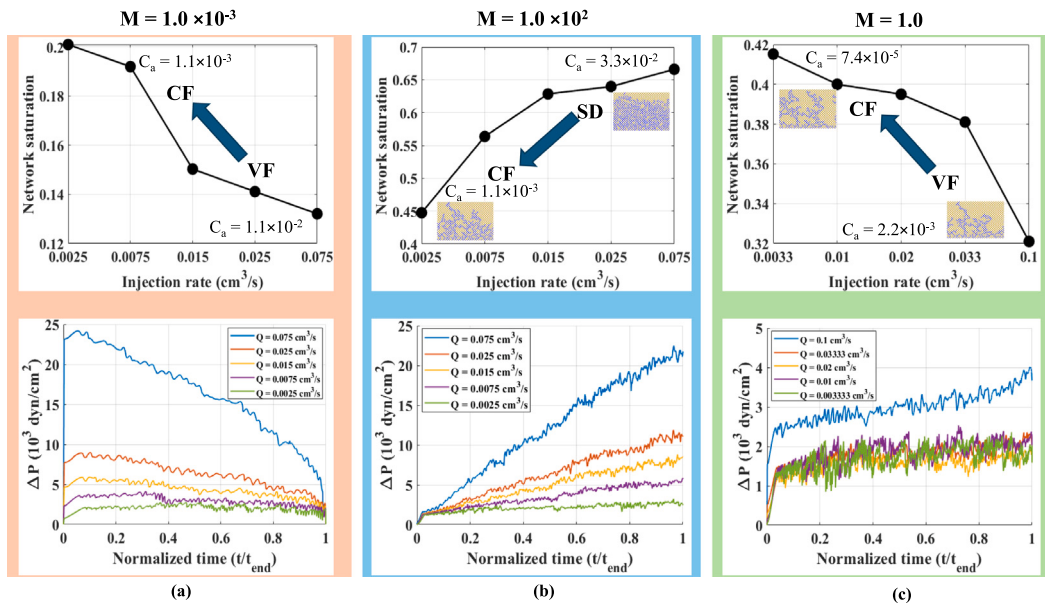


Fig. 10. Network saturation and pressure variations for different viscosity ratios and injection rates. (a–c) Saturation at breakthrough vs. injection rate (cm^3/s) and pressure difference (ΔP) vs. normalized time (t/t_{end}) for viscous fingering ($M = 10^{-3}$), stable displacement ($M = 10^2$), and capillary fingering ($M = 1.0$). Higher injection rates (C_a) lead to viscous fingering, reducing network saturation, while lower C_a increases saturation and shifts the regime to capillary fingering.

pressure data (Fig. 10(a)), where pressure (ΔP) decreases significantly at lower injection rates, signaling the transition from viscous to capillary fingering. Fig. 10(b) presents the network saturation and pressure variation for $M = 100$. At high injection rates, the flow exhibits stable displacement. As the injection rate decreases, capillary forces become increasingly significant, leading to a transition to capillary fingering. This shift in flow regime is clearly visible in Fig. 10(b). Fig. 10(b) shows the evolution of the pressure difference (ΔP) across different injection rates, highlighting a reduction in ΔP as the injection rate decreases. Lastly, network saturation during invasion with viscosity-matched fluids ($M = 1.0$) as a function of injection rate is illustrated in Fig. 10(c). At low capillary numbers, capillary force dominates, and the invading phase follows the path of least resistance. As the injection rate increases, viscous forces become more dominant, leading to a transition toward the viscous fingering regime and a corresponding decrease in network saturation. Fig. 10(c) also presents the pressure difference (ΔP) across all injection rates. For most cases, ΔP fluctuates around $1.5 \times 10^3 \text{ dyn/cm}^2$, suggesting that moderate changes in injection rate do not significantly affect pressure behavior, thus maintaining the capillary fingering regime in matching-viscosity fluids. However, at the highest injection rate, ΔP rises to approximately $3 \times 10^3 \text{ dyn/cm}^2$, indicating a shift in the displacement regime.

5.2.2. Effect of contact angle

In this section, we study the effect of contact angles (θ) on the flow pattern and pressure variation for different viscosity ratios. Fig. 11(a) illustrates the evolution of the pressure difference (ΔP) for $M < 1$ and $Q = 0.025 \text{ cm}^3/\text{s}$. As θ increases, capillary pressure in the throats decrease, and lowers the pressure needed to drive the invading phase to the outlet. During invasion, at $\theta = 90^\circ$, the invading phase develops more widespread fingers compared to $\theta = 0^\circ$ due to the absence of capillary force in the throats. For $M = 100$ and $Q = 0.025 \text{ cm}^3/\text{s}$, the pressure difference decreases as θ increases (Fig. 11(b)), with a more significant reduction compared to $M < 1$. As capillary pressure diminishes in all throats, lesser inlet pressure is needed to drive the invading phase. When P_c reaches zero, the invading phase fills all the throats uniformly, especially when a more viscous fluid invades a network saturated with a less viscous fluid. Fig. 11 (c) shows pressure

evolutions for $M = 1.0$ and $Q = 0.0033 \text{ cm}^3/\text{s}$ under varying contact angles. In this regime, capillary forces dominate for $\theta < 90^\circ$, but vanish when $\theta = 90^\circ$. With equal viscosities, ΔP approaches zero, and minimal pressure is needed to displace the defending phase.

5.3. Isothermal simulations with surfactants

The influence of surfactants on the flow pattern and pressure evolution for viscosity ratio of $M < 1$ without applying heat to the network is first analyzed. This represents an isothermal surfactant flooding case. As shown in the previous sections (Fig. 8(a)), the viscous fingering case $M < 1$ is the least favorable regime since only a few thin fingers are developed throughout the network and the overall saturation is poor ($S = 0.14\text{--}0.26$). By adding surfactant, we aim to show that saturation could be improved. The simulations were conducted based on water and hexadecane oil which have viscosities of 0.01 and 0.0347 Poise, respectively. The water is presumed to be supplemented with the cationic surfactant octadecyl-trimethyl-ammonium bromide ($C_{18}\text{TAB}$). Meanwhile, hexadecanol ($C_{16}\text{OH}$) is added to the oil phase as a co-surfactant. At room temperature (25°C), the surfactant-decorated water–oil interface is hydrophilic ($\theta = 120^\circ$). The curvature of both surfactant-infused and surfactant-free interfaces is unaffected by the spatial dimensions of the capillary [43], implying that the random size distribution of the network does not influence the meniscus curvature. Furthermore, this behavior is independent of the sequence in which the liquids invade or the orientation of the porous medium relative to gravity, suggesting that contact line hysteresis and gravitational effects play an insignificant role.

In our model, surfactant diffusion is neglected based on both physical and operational considerations. First, both the aqueous ($C_{18}\text{TAB}$) and oil (hexadecanol) phases were prepared at or above their respective CMCs. At concentrations exceeding the CMC, the bulk surfactant concentration remains effectively constant due to micelle formation, and any local depletion near interfaces is rapidly replenished from the micellar reservoir. This minimizes the influence of concentration gradients on surface tension and wettability, justifying the assumption of uniform surfactant concentration in the bulk phases. Second, the injection rate is selected to ensure a flow Péclet number $\text{Pe}_F \approx 1$, where

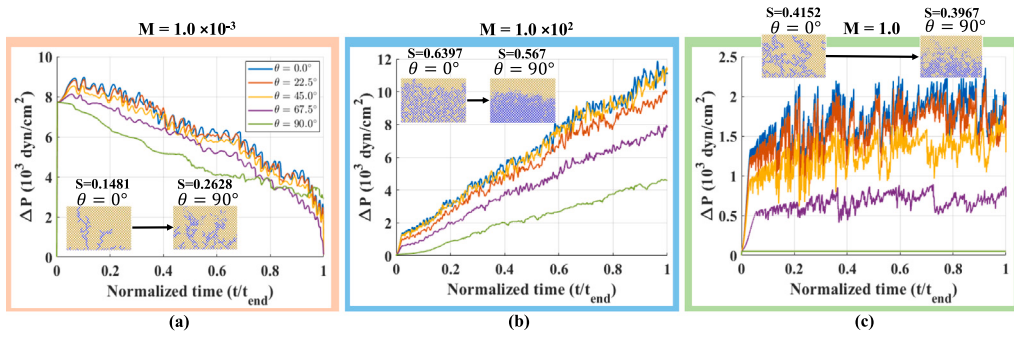


Fig. 11. Effect of contact angle on pressure difference (ΔP) for different viscosity ratios and θ values. (a) For $M < 1$, increasing θ reduces capillary pressure in the throats, lowering the inlet pressure required for invasion. (b) For $M = 100$, the reduction in pressure difference with increasing θ is more pronounced, leading to a more uniform invasion pattern as capillary forces diminish. (c) For $M = 1.0$, capillary forces dominate for $\theta < 90^\circ$ but vanish at $\theta = 90^\circ$, minimizing the pressure needed for displacement.

$\text{Pe}_F = \frac{UL}{D_b}$, with $U = \frac{Q}{A_c}$, L as the throat length, and D_b the surfactant diffusivity. Under this Péclet number regime, surfactant transport is equally dominated by both convection, and diffusion.

Fig. 12 compares the invasion results for water invading the network ($M = 0.287$) with and without surfactants, injected from the bottom side at $Q = 0.0025 \text{ cm}^3/\text{s}$ (chosen such that $\text{Pe}_F \approx 1$). Figs. 12(a and b) show flow patterns with and without surfactants and Fig. 12(c) shows corresponding pressure evolutions (ΔP). It is evident from the invasion pattern and increase in the network saturation that surfactants dramatically influence the displacement pattern under this unfavorable mobility condition ($M < 1$). Surfactants facilitate the invasion by reducing capillary resistance, leading to a more uniform front, lower pressure requirements, and improved displacement. The results for the no-surfactant case reveal a capillary fingering regime, as discussed in Section 5.2.1. This regime also can be identified from the pressure evolution (blue lines) depicted in Fig. 12(c). However, the introduction of the surfactants leads to a substantial reduction in capillary forces, driven by changes in σ and θ . As a result, the invasion front is partially stabilized, making the regime resemble a stable displacement regime. The finger width is significantly larger during surfactant invasion compared to the case without surfactants, and the network saturation is increased by 30%. Fig. 12(c) also indicates that surfactant flooding led to a notable reduction in ΔP due to decrease in surface tension and capillary pressure.

Additionally, Figs. 12(d-f) present the displacement pattern and pressure evolution at a high injection rate of $Q = 0.25 \text{ cm}^3/\text{s}$. Fig. 12(d) shows a viscous fingering regime resulting from the high injection rate. With the introduction of surfactants, as seen in Fig. 12(e), the fingers exhibit slight expansion. However, unlike the case of a low injection rate, the overall flow patterns are less affected by the surfactants. This indicates that the impact of surfactant flooding depends on the injection rate. High flow rates results in advection-dominated surfactant flooding. Here capillary forces become negligible, and altering the capillary force by reducing σ and θ do not influence the displacement pattern considerably. Under these conditions, extreme viscous fingering occurs, characterized by a high pressure difference (ΔP , orange line), and the dominance of viscous forces over capillary forces.

Next, we examine a case with a favorable mobility ratio ($M > 1$) and low injection rate ($Q = 0.0025 \text{ cm}^3/\text{s}$). Under this condition, capillary fingering dominates (Section 5.2.1) in free-surfactant invasion. Nonetheless, the surfactant modifies wettability from oil-wet to water-wet, making water invasion more favorable. A key outcome of surfactant action is the reduction in the amount of trapped oil due to an increase in the effective capillary number (Figs. 13(a-b)). Therefore, comparing the network saturation values at the end of the simulations shows an increase from 0.358 to 0.65 with surfactant. This increase in water saturation arises from the wettability and surface tension change.

5.4. Simulations with temperature-sensitive surfactants

In the previous section, we showed that at high injection rates, under unfavorable viscosity ratio ($M < 1$), viscous forces were dominant. Modifying surface tension is somewhat ineffective as the increase in saturation is minimal and the flow pattern is largely unchanged (Fig. 12(e)). However, in this section, the coupled two-phase flow/thermal model is used to investigate the influence of temperature-sensitive surfactants on flow patterns and pressure evolution. By using temperature-sensitive surfactants, we actively control the wettability and interfacial tension based on the throat temperature, as described in Section 2. The simulations involve the two-phase flow of water and hexadecane oil with densities of 1 g/cm^3 and 0.77 g/cm^3 , specific heats of 4.18 J/g K and 2 J/g K , and thermal conductivities of 0.006 W/cm K and 0.0014 W/cm K , respectively. Water mixed with $C_{18}\text{TAB}$ and hexadecanol ($C_{16}\text{OH}$) is mixed with the oil phase as a co-surfactant. During heating, the $C_{18}\text{TAB}$ surfactant molecules adsorb onto the throat walls, hydrophobizing the surface (the meniscus bulges toward the oil phase). In contrast, cooling causes surfactant desorption due to interfacial freezing and growth of the interfacial area.

As discussed in the previous section, at a high flow rate ($Q = 0.25 \text{ cm}^3/\text{s}$), the effects of surfactants on the capillary forces become negligible compared to viscous forces (Fig. 12(e)). Thus, at high injection rate surfactant flooding could potentially be improved by employing temperature-sensitive surfactants. This provides the ability to change the wettability and interfacial tension of the menisci in the throats by altering the temperature field across the network. Figs. 14(a-c) show the invasion patterns at high flow rate ($Q = 0.25 \text{ cm}^3/\text{s}$) water flooding, with the viscosity ratio of $M=0.288$, with and without surfactants. The thermal model applies a constant heat rate ($Q_t = 0.01 \text{ W}$) at the inlet (bottom) of the network to evaluate the influence of heat on throat temperature and its dependence on throat saturation in a two-way coupled manner. As shown in Fig. 14, when the injection rate is $Q = 0.25 \text{ cm}^3/\text{s}$, a fingering pattern develops during both water flooding and isothermal surfactant flooding. This phenomenon arises due to the significant pressure difference and the minimal influence of capillary forces within the network. However, when the surfactants are temperature-sensitive (by using the thermal model) a noticeable enhancement in the invasion pattern is observed, particularly at the lower section of the network.

In the temperature sensitive surfactant case, the displacement is initially stabilized and formation of fingers is only delayed. Fingers do eventually form in the network far from the inlet. This occurs because the heat applied at the inlet is not strong enough to alter the contact angle, capillary pressure, and ultimately the flow pattern in the upper section of the network. Consequently, the surface tension and contact angle remain unchanged in the top half of the network compared to the

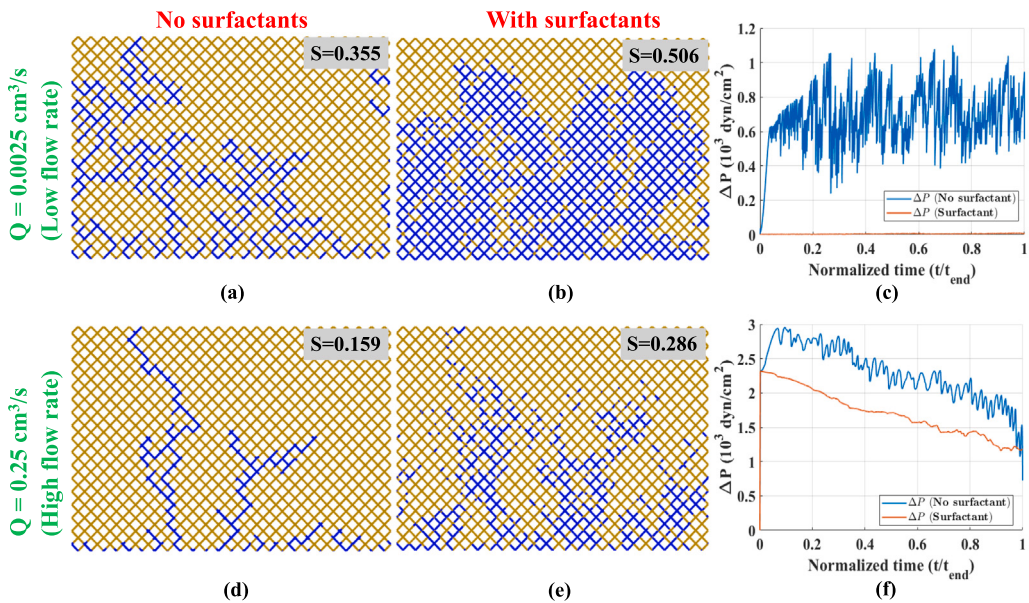


Fig. 12. Effect of surfactants on pressure difference (ΔP), and invasion pattern for different injection rates, and $M = 0.288$. At a low injection rate ($Q = 0.0025 \text{ cm}^3/\text{s}$), surfactants significantly alter the displacement pattern by reducing capillary resistance, leading to a more uniform front, lower pressure requirements, and increased network saturation. However, at a high injection rate ($Q = 0.25 \text{ cm}^3/\text{s}$), where viscous forces dominate, capillary forces become negligible, and surfactants have a minimal impact on the flow pattern.

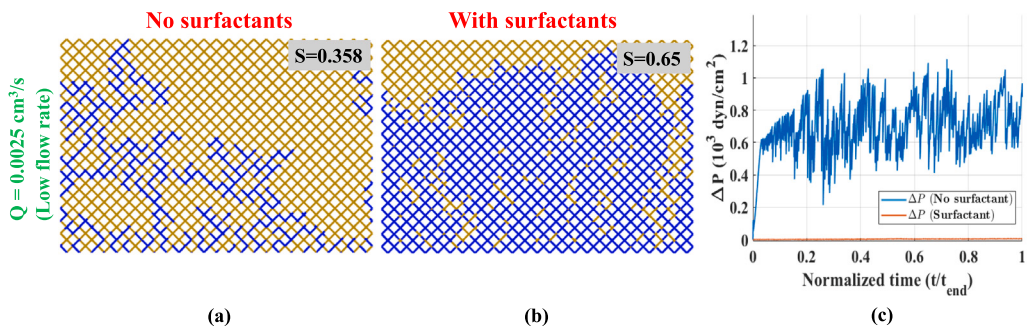


Fig. 13. Effect of surfactants on pressure difference (ΔP), and invasion pattern for $M = 3.47$. In the presence of surfactants, wettability shifts from oil-wet to water-wet, reducing the amount of trapped oil and increasing the effective capillary number. This leads to a higher final water saturation (0.65 compared to 0.358 without surfactants).

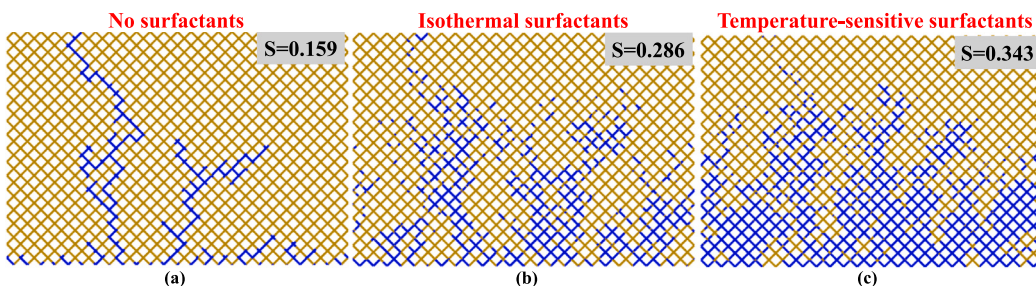


Fig. 14. Effect of temperature-sensitive surfactants on the invasion pattern at $M = 0.288$, $Q = 0.25 \text{ cm}^3/\text{s}$, and $Q_t = 0.01 \text{ W}$. The fingering pattern persists in both water flooding and isothermal surfactant flooding (a, b) due to the dominance of viscous forces. However, with temperature-sensitive surfactants (c), the invasion pattern improves, especially in the lower section of the network, leading to a 53.6% and 46.6% increase in network saturation compared to cases without surfactants and with isothermal surfactants, respectively.

isothermal case. Therefore, the effect of heat rate on the displacement pattern must be characterized.

Fig. 15 illustrates the invasion patterns across the pore network, presented as contours of temperature (top row) and contact angle (bottom row) for applied heat rates of 0.01 W, 0.05 W, and 0.1 W. Breakthrough (the moment the invading phase reaches the top boundary) can occur

even through a single advancing finger, and therefore may not be distinctly observable in all patterns.

As seen in the temperature distributions, the applied heat at the bottom of the network raises the temperature of the throats near the inlet (shown in red). As the heat propagates towards the network outlet, the throat temperature decreases due to the outlet being maintained

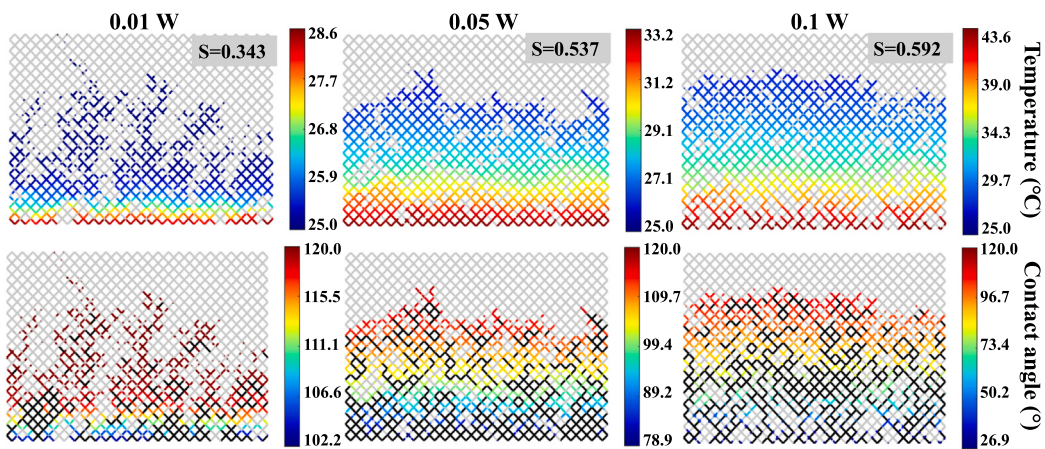


Fig. 15. Effect of applied heat rate on temperature, and contact angle distributions at $M = 0.288$ and $Q = 0.25 \text{ cm}^3/\text{s}$. The first, and second rows show the temperature, and contact angle distributions for heat rates of 0.01 W , 0.05 W , and 0.1 W . The temperature increases near the inlet and decreases toward the outlet, while the contact angle decreases with rising temperature. Higher heat rates lead to reduced contact angles, increased saturation, and a shift from viscous fingering to stable displacement. At 0.1 W , viscous fingering occurs near the inlet, transitioning to stable displacement toward the middle and outlet.

at ambient temperature (25° C), establishing a vertical temperature gradient. Since the contact angle is inversely related to temperature (see Section 2), this gradient results in spatially varying wettability, lower contact angles near the inlet and higher contact angles toward the outlet. This controllable temperature-driven variation in contact angle plays a central role in determining the local capillary pressure and, consequently, the invasion dynamics.

In the contact angle distributions, black regions indicate throats that are completely filled and lack a meniscus. As the applied heat increases, the minimum contact angle in the network decreases substantially (by 73.6% from 0.01 W to 0.1 W), signifying a shift toward more hydrophilic behavior near the heated inlet region. This spatial variation in wettability directly influences the invasion pattern. At low heat rates (0.01 W), the temperature and contact angle gradients are concentrated near the inlet, and the network exhibits classic viscous fingering characterized by broad fingers. The contact angle in these regions remains well below 90° , sustaining high capillary pressures that reinforce finger formation.

At an intermediate heat rate (0.05 W), the invasion pattern shifts significantly. The contact angle in the network's mid-region rises to approximately 90° , reducing capillary pressure to near zero. This eliminates the capillary barriers that otherwise confine the invading fluid to narrow pathways, enabling more uniform and stable displacement. This transition from viscous fingering to stable displacement is a direct consequence of the wettability modification caused by temperature-sensitive surfactants. By tuning the contact angle via local heating, it is possible to suppress fingering instabilities and promote stable displacement patterns.

At the highest heat rate (0.1 W), however, a nonmonotonic behavior is observed. The contact angle near the inlet drops to approximately 27° , drastically increasing local capillary pressure. This enhances viscous fingering near the inlet, as water preferentially invades paths of least resistance. However, further into the network, the contact angle again approaches 90° , shifting the flow regime back to stable displacement. Thus, the interplay between thermal input, wettability variation, and invasion regime is clearly evident in Fig. 15.

Additionally, the transition from viscous fingering to stable displacement increases the time required for invasion, allowing the temperature gradient to distribute more uniformly throughout the network. This uniformity is further supported by the lower effective thermal resistance of throats with higher water saturation. In summary, the spatial variation in contact angle which is driven by temperature gradients enables dynamic control over local wettability. This control governs the

flow regime transitions observed in the network, including suppression or promotion of viscous fingering and the onset of stable displacement. These findings highlight the potential of temperature-sensitive surfactants to actively manipulate multiphase flow in porous media by tailoring the local wetting properties of the system.

6. Conclusions

This study investigates the reversible switching of meniscus curvature at surfactant-decorated oil-water interfaces, driven by temperature-induced wettability changes. We developed a coupled thermal/flow pore-scale model to capture this behavior, incorporating temperature-sensitive surfactants and varying temperatures. We showed that temperature-induced wettability transitions can enhance transport behavior in porous media and optimize flow processes in various applications.

Two-phase flow simulations were conducted without thermal models or surfactants to investigate the impact of injection rate, and contact angle on invasion patterns and network saturation. Results showed that injection rate influences regime transitions, with higher rates promoting viscous fingering and lower rates favoring capillary fingering. Furthermore, the contact angle variation enables controlling the capillary forces driving displacement. These findings underscore the critical physical parameters in dictating the behavior of multiphase flow systems.

Further, the simulations conducted in this study demonstrated the significant role of surfactants in modifying flow patterns, pressure evolution, and network saturation under varying conditions. For unfavorable mobility ratios ($M < 1$), surfactants reduce capillary forces by altering surface tension and contact angle, resulting in partial stabilization of the invasion front and increased network saturation by 30%. Conversely, for favorable mobility ratios ($M > 1$), surfactants enhance water saturation from 0.358 to 0.65 by shifting wettability and increasing the effective capillary number. However, at high injection rates, surfactants failed to mitigate extreme viscous fingering due to the dominance of viscous forces.

Finally, the study investigates the effects of temperature-sensitive surfactants on two-phase flow and thermal behavior in porous networks under varying heat rates. Simulation results showed that temperature-sensitive surfactants can effectively modify wettability and interfacial tension, significantly influencing flow regimes. At high flow rates ($Q = 0.25 \text{ cm}^3/\text{s}$), where viscous forces dominate, the surfactant temperature sensitivity enables active control over the invasion pattern. Increasing

heat rates enhances throat temperatures and reduces contact angles, transitioning flow from viscous fingering to stable displacement. Notably, at the moderate heat rate ($Q_t = 0.05 \text{ W}$), the displacement pattern stabilizes due to reduced capillary forces, promoting uniform saturation which resulted in 31.2% increase in water saturation compared to the low heat rate. However, excessive heating ($Q_t = 0.1 \text{ W}$) reintroduces fingering near the inlet due to elevated capillary pressure. These findings demonstrated that regime transitions in two-phase flow, traditionally achieved by adjusting flow rate or fluid/substrate properties, can also be induced through localized thermal control. By coupling thermal actuation with surfactant-modified interfaces, our study provides a reversible and practical method to tune displacement patterns and enhance transport in porous media.

CRediT authorship contribution statement

Amirhosein Sarchami: Writing – original draft, Visualization, Validation, Software, Methodology, Investigation, Formal analysis. **Kishan Bellur:** Writing – review & editing, Supervision, Project administration, Methodology, Conceptualization.

Declaration of competing interest

The authors declare that they have no known competing financial interests or personal relationships that could have appeared to influence the work reported in this paper.

Acknowledgment

The authors would like to thank Saaras Pakanati for valuable assistance with the visualization and graphical representation used in this work.

Appendix A. Supplementary data

Supplementary material related to this article can be found online at <https://doi.org/10.1016/j.colsurfa.2025.138678>.

Data availability

Data will be made available on request.

References

- [1] L.M. Giudici, A.Q. Raeini, T. Akai, M.J. Blunt, B. Bijeljic, Pore-scale modeling of two-phase flow: A comparison of the generalized network model to direct numerical simulation, *Phys. Rev. E* 107 (3) (2023) 035107, <http://dx.doi.org/10.1103/PhysRevE.107.035107>.
- [2] Q. Wang, Z. Jia, L. Cheng, B. Li, P. Jia, Y. Lan, D. Dong, F. Qu, Characterization of Flow Parameters in Shale Nano-Porous Media Using Pore Network Model: A Field Example from Shale Oil Reservoir in Songliao Basin, China, *Energies* 16 (14) (2023) 5424, <http://dx.doi.org/10.3390/en16145424>.
- [3] M. Arshadi, M. Gesho, T. Qin, L. Goual, M. Piri, Impact of mineralogy and wettability on pore-scale displacement of NAPLs in heterogeneous porous media, *J. Contam. Hydrol.* 230 (2020) 103599, <http://dx.doi.org/10.1016/j.jconhyd.2020.103599>.
- [4] D. Picchii, I. Battiatto, Scaling of two-phase water-steam relative permeability and thermal fluxes in porous media, *Int. J. Multiph. Flow* 129 (2020) 103257, <http://dx.doi.org/10.1016/j.ijmultiphaseflow.2020.103257>.
- [5] J. Liu, K. Duan, Q. Zhang, Y. Zheng, H. Cao, Y. Zhang, Pore-scale insights into CO₂-water two-phase flow and implications for benefits of geological carbon storage, *Adv. Water Resour.* 191 (2024) 104780, <http://dx.doi.org/10.1016/j.advwatres.2024.104780>.
- [6] X. Shu, Y. Wu, X. Zhang, F. Yu, Experiments and models for contaminant transport in unsaturated and saturated porous media – A review, *Chem. Eng. Res. Des.* 192 (2023) 606–621, <http://dx.doi.org/10.1016/j.cherd.2023.02.022>.
- [7] E.F. Médici, J.S. Allen, Evaporation, two phase flow, and thermal transport in porous media with application to low-temperature fuel cells, *Int. J. Heat Mass Transfer* 65 (2013) 779–788, <http://dx.doi.org/10.1016/j.ijheatmasstransfer.2013.06.035>.
- [8] B. Thibault, S. Aghajanzadeh, A. Sultana, C. Ratti, S. Khaliloufi, Characteristics of Open and Closed Pores, Their Measurement Techniques and Exploitation in Dehydrated Food Products, *Food Eng. Rev.* (2024) <http://dx.doi.org/10.1007/s12393-024-09376-4>.
- [9] Q. Chen, Z. Niu, H. Li, K. Jiao, Y. Wang, Recent progress of gas diffusion layer in proton exchange membrane fuel cell: Two-phase flow and material properties, *Int. J. Hydrog. Energy* 46 (12) (2021) 8640–8671, <http://dx.doi.org/10.1016/j.ijhydene.2020.12.076>.
- [10] F.J. Carrillo, I.C. Bourg, Modeling Multiphase Flow Within and Around Deformable Porous Materials: A Darcy-Brinkman-Biot Approach, *Water Resour. Res.* 57 (2) (2021) <http://dx.doi.org/10.1029/2020WR028734>, e2020WR028734.
- [11] R.T. White, S.H. Eberhardt, Y. Singh, T. Haddow, M. Dutta, F.P. Orfino, E. Kjeang, Four-dimensional joint visualization of electrode degradation and liquid water distribution inside operating polymer electrolyte fuel cells, *Sci. Rep.* 9 (1) (2019) 1843, <http://dx.doi.org/10.1038/s41598-018-38464-9>.
- [12] S. Thiele, T. Fürstenhaupt, D. Banham, T. Hutzenlaub, V. Birss, C. Ziegler, R. Zengerle, Multiscale tomography of nanoporous carbon-supported noble metal catalyst layers, *J. Power Sources* 228 (2013) 185–192, <http://dx.doi.org/10.1016/j.jpowsour.2012.11.106>.
- [13] S. Foroughi, B. Bijeljic, Y. Gao, M.J. Blunt, Incorporation of Sub-Resolution Porosity Into Two-Phase Flow Models With a Multiscale Pore Network for Complex Microporous Rocks, *Water Resour. Res.* 60 (4) (2024) <http://dx.doi.org/10.1029/2023WR036393>, e2023WR036393.
- [14] S. Konangi, N.K. Palakurthi, N.K. Karadimitriou, K. Comer, U. Ghia, Comparison of pore-scale capillary pressure to macroscale capillary pressure using direct numerical simulations of drainage under dynamic and quasi-static conditions, *Adv. Water Resour.* 147 (2021) 103792, <http://dx.doi.org/10.1016/j.advwatres.2020.103792>.
- [15] S. Wang, P. Liu, H. Zhao, Y. Zhang, A novel method for calculating the dynamic capillary force and correcting the pressure error in micro-tube experiment, *Sci. Rep.* 7 (1) (2017) 16590, <http://dx.doi.org/10.1038/s41598-017-16870-9>.
- [16] A. D’Orazio, A. Karimipour, R. Ranjbarzadeh, Lattice Boltzmann Modelling of Fluid Flow through Porous Media: A Comparison between Pore-Structure and Representative Elementary Volume Methods, *Energies* 16 (14) (2023) 5354, <http://dx.doi.org/10.3390/en16145354>.
- [17] Q. Xiong, T.G. Baychev, A.P. Jivkov, Review of pore network modelling of porous media: Experimental characterisations, network constructions and applications to reactive transport, *J. Contam. Hydrol.* 192 (2016) 101–117, <http://dx.doi.org/10.1016/j.jconhyd.2016.07.002>.
- [18] I. Fatt, The Network Model of Porous Media, *Trans. AIME* 207 (01) (1956) 144–181, <http://dx.doi.org/10.2118/574-G>.
- [19] E. Aker, K. Jørgen Måløy, A. Hansen, G.G. Batrouni, A two-dimensional network simulator for two-phase flow in porous media, *Transp. Porous Media* 32 (1998) 163–186.
- [20] Y. Yang, K. Wang, L. Zhang, H. Sun, K. Zhang, J. Ma, Pore-scale simulation of shale oil flow based on pore network model, *Fuel* 251 (2019) 683–692, <http://dx.doi.org/10.1016/j.fuel.2019.03.083>.
- [21] B. Gharedaghloo, J.S. Price, F. Rezanezhad, W.L. Quinton, Evaluating the hydraulic and transport properties of peat soil using pore network modeling and X-ray micro computed tomography, *J. Hydrol.* 561 (2018) 494–508, <http://dx.doi.org/10.1016/j.jhydrol.2018.04.007>.
- [22] H. Nakajima, S. Iwasaki, T. Kitahara, Pore network modeling of a microporous layer for polymer electrolyte fuel cells under wet conditions, *J. Power Sources* 560 (2023) 232677, <http://dx.doi.org/10.1016/j.jpowsour.2023.232677>.
- [23] E. Unsal, P. Hammond, M. Schneider, Effects of Surfactant on Wettability and Oil Recovery in a Pore Network Model, in: IOR 2011 - 16th European Symposium on Improved Oil Recovery, European Association of Geoscientists & Engineers, 2011, p. cp, <http://dx.doi.org/10.3997/2214-4609.201404749>.
- [24] R. Cui, S.M. Hassanzadeh, S. Sun, Pore-network modeling of flow in shale nanopores: Network structure, flow principles, and computational algorithms, *Earth-Sci. Rev.* 234 (2022) 104203, <http://dx.doi.org/10.1016/j.earscirev.2022.104203>.
- [25] H. Fyhn, S. Sinha, S. Roy, A. Hansen, Rheology of Immiscible Two-phase Flow in Mixed Wet Porous Media: Dynamic Pore Network Model and Capillary Fiber Bundle Model Results, *Transp. Porous Media* 139 (3) (2021) 491–512, <http://dx.doi.org/10.1007/s11242-021-01674-3>.
- [26] P.S. Hammond, E. Unsal, A Dynamic Pore Network Model for Oil Displacement by Wettability-Altering Surfactant Solution, *Transp. Porous Media* 92 (3) (2012) 789–817, <http://dx.doi.org/10.1007/s11242-011-9933-4>.
- [27] Y. Sun, K. Gao, Z. Yu, Y. Fang, Y. Chang, A. Chen, C. Dai, C. Wang, C. Chen, Y. Xu, Dynamic imbibition with aid of surfactant in tight oil fracture network model, *J. Pet. Sci. Eng.* 193 (2020) 107393, <http://dx.doi.org/10.1016/j.petrol.2020.107393>.
- [28] Y. Yao, M. Wei, W. Kang, A review of wettability alteration using surfactants in carbonate reservoirs, *Adv. Colloid Interface Sci.* 294 (2021) 102477, <http://dx.doi.org/10.1016/j.cis.2021.102477>.
- [29] H. Esfandyari, S.R. Shadizadeh, F. Esmailzadeh, A. Davarpanah, Implications of anionic and natural surfactants to measure wettability alteration in EOR processes, *Fuel* 278 (2020) 118392, <http://dx.doi.org/10.1016/j.fuel.2020.118392>.

- [30] S. Ahmadi, M. Hosseini, E. Tangestani, S.E. Mousavi, M. Niazi, Wettability alteration and oil recovery by spontaneous imbibition of smart water and surfactants into carbonates, *Pet. Sci.* 17 (3) (2020) 712–721, <http://dx.doi.org/10.1007/s12182-019-00412-1>.
- [31] A. Ratanpara, M. Kim, Wettability Alteration Mechanisms in Enhanced Oil Recovery with Surfactants and Nanofluids: A Review with Microfluidic Applications, *Energies* 16 (24) (2023) 8003, <http://dx.doi.org/10.3390/en16248003>.
- [32] C.A. López, A.H. Hirsa, Fast focusing using a pinned-contact oscillating liquid lens, *Nat. Photonics* 2 (10) (2008) 610–613, <http://dx.doi.org/10.1038/nphoton.2008.198>.
- [33] S. Shi, B. Qian, X. Wu, H. Sun, H. Wang, H.-B. Zhang, Z.-Z. Yu, T.P. Russell, Self-Assembly of MXene-Surfactants at Liquid-Liquid Interfaces: From Structured Liquids to 3D aerogels, *Angew. Chem. Int. Ed.* 58 (50) (2019) 18171–18176, <http://dx.doi.org/10.1002/anie.201908402>.
- [34] J. Li, X. Zhou, J. Li, L. Che, J. Yao, G. McHale, M.K. Chaudhury, Z. Wang, Topological liquid diode, *Sci. Adv.* 3 (10) (2017) eaao3530, <http://dx.doi.org/10.1126/sciadv.aao3530>.
- [35] B.B. Patel, D.J. Walsh, D.H. Kim, J. Kwok, B. Lee, D. Guironnet, Y. Diao, Tunable structural color of bottlebrush block copolymers through direct-write 3D printing from solution, *Sci. Adv.* 6 (24) (2020) eaaz7202, <http://dx.doi.org/10.1126/sciadv.aaz7202>.
- [36] B. Ma, L. Shan, B. Dogruoz, D. Agonafer, Evolution of Microdroplet Morphology Confined on Asymmetric Micropillar Structures, *Langmuir* 35 (37) (2019) 12264–12275, <http://dx.doi.org/10.1021/acs.langmuir.9b01410>.
- [37] G. Kitahara, S. Inoue, T. Higashino, M. Ikawa, T. Hayashi, S. Matsuoka, S. Arai, T. Hasegawa, Meniscus-controlled printing of single-crystal interfaces showing extremely sharp switching transistor operation, *Sci. Adv.* 6 (41) (2020) eabc8847, <http://dx.doi.org/10.1126/sciadv.abc8847>.
- [38] L.M. Ostertag, X. Ling, K.F. Domke, S.H. Parekh, M. Valtiner, Characterizing the hydrophobic-to-hydrophilic transition of electrolyte structuring in proton exchange membrane mimicking surfaces, *Phys. Chem. Chem. Phys.* 20 (17) (2018) 11722–11729, <http://dx.doi.org/10.1039/C8CP01625A>.
- [39] J. Rafiee, M.A. Rafiee, Z.-Z. Yu, N. Koratkar, Superhydrophobic to Superhydrophilic Wetting Control in Graphene Films, *Adv. Mater.* 22 (19) (2010) 2151–2154, <http://dx.doi.org/10.1002/adma.200903696>.
- [40] R. Barni, S. Zanini, D. Beretta, C. Riccardi, Experimental study of hydrophobic/hydrophilic transition in SF₆ plasma interaction with polymer surfaces, *Eur. Phys. J. Appl. Phys.* 38 (3) (2007) 263–268, <http://dx.doi.org/10.1051/epjap:2007075>.
- [41] M. Anyfantakis, D. Baigl, Dynamic Photocontrol of the Coffee-Ring Effect with Optically Tunable Particle Stickiness, *Angew. Chem. Int. Ed.* 53 (51) (2014) 14077–14081, <http://dx.doi.org/10.1002/anie.201406903>.
- [42] R. Lenormand, C. Zarcone, A. Sarr, Mechanisms of the displacement of one fluid by another in a network of capillary ducts, *J. Fluid Mech.* 135 (1983) 337–353.
- [43] L. Shool, A.V. Butenko, S.R. Liber, Y. Rabin, E. Sloutskin, Anomalous Temperature-Controlled Concave–Convex Switching of Curved Oil–Water Menisci, *J. Phys. Chem. Lett.* 12 (29) (2021) 6834–6839, <http://dx.doi.org/10.1021/acs.jpclett.1c01937>.
- [44] H. Wu, M. Veyskarami, M. Schneider, R. Helmig, A New Fully Implicit Two-Phase Pore-Network Model by Utilizing Regularization Strategies, *Transp. Porous Media* 151 (1) (2024) 1–26, <http://dx.doi.org/10.1007/s11242-023-02031-2>.
- [45] E.W. Washburn, The Dynamics of Capillary Flow, *Phys. Rev.* 17 (3) (1921) 273–283, <http://dx.doi.org/10.1103/PhysRev.17.273>.
- [46] V. Surasani, T. Metzger, E. Tsotsas, Consideration of heat transfer in pore network modelling of convective drying, *Int. J. Heat Mass Transfer* 51 (9–10) (2008) 2506–2518, <http://dx.doi.org/10.1016/j.ijheatmasstransfer.2007.07.033>.
- [47] M. Ferer, C. Ji, G.S. Bromhal, J. Cook, G. Ahmadi, D.H. Smith, Crossover from capillary fingering to viscous fingering for immiscible unstable flow: Experiment and modeling, *Phys. Rev. E* 70 (1) (2004) 016303, <http://dx.doi.org/10.1103/PhysRevE.70.016303>.